

# My paper on the cosmic microwave background and formation of structures in our Universe

V. A. Vikenes<sup>1</sup>

Institute of Theoretical Astrophysics, University of Oslo, 0315 Oslo, Norway  
e-mail: v.a.vikenes@astro.uio.no

May 5, 2023

## ABSTRACT

The code for this project can be found on my GitHub repository: <https://github.com/Vikenes/AST5220/>

**Key words.** cosmic microwave background – large-scale structure of Universe

## 1. Introduction

Write an introduction here. Give context to the paper. Citations to relevant papers. You only need to do this in the end for the last milestone.

## 2. Milestone I

In this section we will examine the evolution of the Universe's uniform background. Our primary objective is to develop methods for computing the Hubble parameter and related time- and distance measures. These methods provide a first step towards further investigations and modelling of the early Universe. To compute the background cosmology, we will solve ordinary differential equations (ODEs) numerically, using cosmological parameters obtained from the Planck Collaboration (Planck Collaboration et al. 2020). The parameters we will use are listed in Eq. (A.1) in Appendix A. One crucial aspect in the process is validating our model. We will therefore develop some simple methods for comparing our result. This will mainly involve considering simplified cases where analytical solutions can be obtained.

Our primary focus in this section concerns methods where the cosmological parameters are given from the start. Another interesting aspect is to use data to constrain cosmological parameters. To do this, we will use data from supernova observations (Betoule et al. 2014), containing luminosity distance associated with different values of redshift. By employing the numerical methods we develop initially, we will try to estimate optimal values of three cosmological parameters, by implement a simple Markov chain Monte Carlo (MCMC) algorithm. The parameters we will be sampling are  $h$ ,  $\Omega_{m0}$  and  $\Omega_{\Lambda0}$ . From these results, we will investigate confidence regions of  $\Omega_{m0}$  and  $\Omega_{\Lambda0}$ , and try to estimate a probability distribution function (PDF) for the Hubble parameter.

### 2.1. Theory

#### 2.1.1. Density parameters and Hubble factor

The Friedmann equation can be written in terms of density parameters,  $\Omega_i \equiv \rho_i/\rho_c$ , where  $\rho_c \equiv 3H^2/8\pi G$  is the critical density. The density of a given species,  $i$ , evolves as (Dodelson 2020, Eq. (2.61))

$$\rho_i(t) \propto a(t)^{-3(1+w_i)}, \quad (1)$$

where we have assumed that the equation of state (EoS) parameter,  $w_i \equiv P_i/\rho_i$  (Dodelson 2020, Eq. 2.60), is constant.  $P_i$  denotes the pressure of the species. We will limit ourselves to consider three types of species in this report: matter, radiation and dark energy. We will only consider baryons and cold dark matter (CDM) for the matter component, which we express as  $\Omega_{m0} = \Omega_{b0} + \Omega_{\text{CDM}0}$ . The subscript 0 is used to refer to today's value. The radiation component we consider is  $\Omega_{r0} = \Omega_{\gamma0} + \Omega_{\nu0}$ , corresponding to photons and neutrinos, respectively. For the dark energy, we only have the cosmological constant  $\Omega_{\Lambda0}$ .

Matter, radiation and dark energy have densities evolving according to Eq. (1) with  $w_i = 0, 1/3$  and  $-1$ , respectively. Neutrinos having  $w = 1/3$  only holds since we will assume that the neutrinos are massless. Curvature can be described by  $w_i = -1/3$ , with  $\Omega_{k0} \equiv -kc^2/H_0^2$ . The parameter  $k$  represents the curvature of the Universe, where  $k = 0$  corresponds to a flat Universe. With these parameters, the Friedmann Equation can be written as (Dodelson 2020, Eq. (3.14))

$$H = H_0 \sqrt{\Omega_{m0}a^{-3} + \Omega_{r0}a^{-4} + \Omega_{k0}a^{-2} + \Omega_{\Lambda0}}, \quad (2)$$

where  $H \equiv \dot{a}/a$  is the Hubble parameter, with the dot denoting a derivative with respect to cosmic time,  $t$ . For the radiation,  $\Omega_{\gamma0}$  and  $\Omega_{\nu0}$  follow from the temperature of the CMB today,  $T_{\text{CMB}0}$ , and the effective number of massless neutrinos,  $N_{\text{eff}}$ . They are given by

$$\Omega_{\gamma0} = 2 \cdot \frac{\pi^2}{30} \frac{(k_b T_{\text{CMB}0})^4}{\hbar^3 c^5} \cdot \frac{8\pi G}{3H_0^2}, \quad (3)$$

$$\Omega_{\nu0} = N_{\text{eff}} \cdot \frac{7}{8} \cdot \left(\frac{4}{11}\right)^{4/3} \Omega_{\gamma0}. \quad (4)$$

The value of  $\Omega_{\Lambda 0}$  is fixed by the requirement that  $H(a = 1) = H_0$ , yielding

$$\Omega_{\Lambda 0} = 1 - (\Omega_{m0} + \Omega_{r0} + \Omega_{k0}). \quad (5)$$

We also introduce the scaled Hubble factor,  $\mathcal{H} \equiv aH$ . Rather than working with the scale factor,  $a(t)$ , we will mainly be working with the logarithm of the scale factor

$$x \equiv \ln a, \quad ' \equiv \frac{d}{dx}. \quad (6)$$

The resulting expression for  $\mathcal{H}(x)$  is thus

$$\mathcal{H}(x) = H_0 \sqrt{\Omega_{m0}e^{-x} + \Omega_{r0}e^{-2x} + \Omega_{k0} + \Omega_{\Lambda 0}e^{2x}}. \quad (7)$$

This form of the Hubble factor is the one we will focus on for the majority of this report. In terms of  $\mathcal{H}(x)$ , the value of the density parameters can be obtained at any given  $x$ , with

$$\Omega_k(x) = \frac{\Omega_{k0}}{\mathcal{H}(x)^2/H_0^2}, \quad (8)$$

$$\Omega_m(x) = \frac{\Omega_{m0}}{e^x \mathcal{H}(x)^2/H_0^2}, \quad (9)$$

$$\Omega_r(x) = \frac{\Omega_{r0}}{e^{2x} \mathcal{H}(x)^2/H_0^2}, \quad (10)$$

$$\Omega_{\Lambda}(x) = \frac{\Omega_{\Lambda 0}}{e^{-2x} \mathcal{H}(x)^2/H_0^2}, \quad (11)$$

From these expressions, we can identify the epochs during which the Universe was dominated by an equal amount of matter and radiation, and by an equal amount of matter and dark energy. These epochs are defined by the time when  $\Omega_m = \Omega_r$  and  $\Omega_m = \Omega_{\Lambda}$ , respectively, and are a valuable asset towards understanding the physics governing the evolution of the Universe. Another time of interest is the onset of acceleration, defined as the time when  $\ddot{a} = 0$ . In terms of  $\mathcal{H}$  and  $x$ , this corresponds to

$$\ddot{a} = \frac{dx}{dt} \frac{da}{dx} = \frac{d \ln a}{dt} \frac{d\mathcal{H}(x)}{dx} = e^{-x} \mathcal{H}(x) \frac{d\mathcal{H}(x)}{dx}. \quad (12)$$

In Sect. 2.1.4 we will derive an expression for  $\mathcal{H}'(x)$ .

### 2.1.2. Conformal time

We now want to relate the Hubble factor to some time variables. The main one we will consider is the conformal time,  $\eta$ . It is a measure of the distance light has been able to travel since  $t = 0$ , where  $t$  is the cosmic time. Using its definition in terms of  $t$  (Dodelson 2020, Eq. (2.90)), we can express it in terms of  $x$  as

$$\eta = \int_0^t \frac{c dt'}{a(t')} = \int_{-\infty}^{x'} \frac{c dx'}{\mathcal{H}(x')}. \quad (13)$$

This leads us to the following differential equation that we will solve numerically

$$\frac{d\eta}{dx} = \frac{c}{\mathcal{H}(x)}. \quad (14)$$

The initial condition we have is  $\eta(-\infty) = 0$ . Noting from Eq. (7) that  $\mathcal{H}(x) \rightarrow H_0 \sqrt{\Omega_{r0}e^{-2x}}$  as  $x \rightarrow -\infty$ , we get an analytical approximation for the initial condition of  $\eta$  at early times

$$\eta(x_{\text{start}}) \approx \int_{-\infty}^{x_{\text{start}}} \frac{c dx'}{H_0 \sqrt{\Omega_{r0}}} e^{x'} = \frac{c}{\mathcal{H}(x_{\text{start}})}. \quad (15)$$

Note that  $\eta(x)\mathcal{H}(x)/c \rightarrow 1$  at low  $x$ , which provides a natural way of validating our implementation.

For the cosmic time,  $t$ , starting from  $H = \dot{a}/a$  and applying the chain rule yields the desired differential equation for  $t(x)$ , which we will solve numerically,

$$\frac{dt}{dx} = \frac{1}{H(x)}. \quad (16)$$

To get an initial condition for  $t$ , we consider the radiation dominating era, with the following integral expression

$$t(x) = \int_{-\infty}^x \frac{dx'}{H(x')}. \quad (17)$$

Comparing with Eq. (15), we see that the two integrands only differ by a factor  $e^x$ . The initial condition for  $t$  is therefore easily seen to be

$$t(x_{\text{start}}) = \frac{1}{2H(x_{\text{start}})}. \quad (18)$$

### 2.1.3. Distance measures

The supernova data we will study has distances measured in terms of luminosity distance,  $d_L$ . Expressing it in terms of the angular distance,  $d_A = ar$ , it becomes

$$d_L(a) = \frac{d_A}{a^2} = \frac{r}{a} \implies d_L(x) = e^{-x}r. \quad (19)$$

Here,  $r$  represents the radial coordinate of the emitted photon. To get an expression for  $r$ , we consider a photon's line-element in spherical coordinates,

$$ds^2 = -c^2 dt^2 + a^2 \left( \frac{dr^2}{1 - kr^2} + r^2 d\theta^2 + r^2 \sin^2 \theta d\phi^2 \right). \quad (20)$$

For photons travelling radially towards us, we have  $d\theta = d\phi = 0$ . Since  $ds^2 = 0$  for photons, integrating the line-element of a photon emitted at,  $(t, r)$ , reaching an observer at  $(t_0, 0)$ , yields

$$\int_0^r \frac{dr'}{\sqrt{1 - kr'^2}} = \int_t^{t_0} \frac{c dt}{a}. \quad (21)$$

The RHS of Eq. (21) is known as the co-moving distance,  $\chi$ , which in terms of conformal time is given as

$$\chi = \int_t^{t_0} \frac{c dt}{a} = \int_x^0 \frac{c dx'}{\mathcal{H}(x')} = \eta(0) - \eta(x). \quad (22)$$

Solving Eq. (21) with respect to  $r$ , we get

$$r = \begin{cases} \chi \cdot \frac{\sin(\sqrt{|\Omega_{k0}|}H_0\chi/c)}{(\sqrt{|\Omega_{k0}|}H_0\chi/c)}, & \Omega_{k0} < 0, \\ \chi, & \Omega_{k0} = 0, \\ \chi \cdot \frac{\sinh(\sqrt{|\Omega_{k0}|}H_0\chi/c)}{(\sqrt{|\Omega_{k0}|}H_0\chi/c)}, & \Omega_{k0} > 0. \end{cases} \quad (23)$$

Eq. (19) can now be used to compute  $d_L$ , and the expression to use depends on the curvature.

#### 2.1.4. Analytical solutions

In Sect. 2.1.2 we discussed how  $\eta(x)$  can be used to test our implementation in the radiation dominating era. To test our solutions in other regimes, we will need the first and second derivative of  $\mathcal{H}(x)$ . To simplify the resulting expressions, we define the function,  $g(x)$ , as the derivative of the term inside the square root in Eq. (7), namely

$$g(x) \equiv -\Omega_{m0}e^{-x} - 2\Omega_{r0}e^{-2x} + 2\Omega_{\Lambda0}e^{2x}. \quad (24)$$

The first two derivatives of  $\mathcal{H}(x)$  are easily seen to be

$$\frac{d\mathcal{H}(x)}{dx} = \frac{H_0^2}{2\mathcal{H}(x)}g(x), \quad (25)$$

$$\frac{d^2\mathcal{H}(x)}{dx^2} = \frac{H_0^2}{2\mathcal{H}(x)} \left[ g'(x) - \frac{1}{2} \left( \frac{H_0 g(x)}{\mathcal{H}(x)} \right)^2 \right]. \quad (26)$$

Now we will consider the situation where the Universe is dominated by a single fluid with a constant EoS parameter,  $w$ . In that case we have  $H(t)^2 \propto \rho_i(t)^2$  (Dodelson 2020, Eq. (3.13)). Using Eq. (1), the Hubble parameter expressed in terms of  $w_i$  becomes

$$H(t)^2 \propto a^{-3(1+w)} \implies \mathcal{H}(x) = c_1 e^{-\frac{3}{2}(1+w)x}, \quad (27)$$

where  $c_1$  is some constant. The reason for doing this, is that both  $c_1$  and the exponential factor drops out when we consider  $\mathcal{H}'(x)/\mathcal{H}(x)$  and  $\mathcal{H}''(x)/\mathcal{H}(x)$ . For different values of  $w_i$ ,  $\mathcal{H}'(x)/\mathcal{H}(x)$  becomes

$$\frac{1}{\mathcal{H}(x)} \frac{d\mathcal{H}}{dx} = -\frac{1+3w}{2} = \begin{cases} -1, & w = 1/3, \\ -1/2, & w = 0, \\ 1, & w = -1. \end{cases} \quad (28)$$

Similarly, the expression for  $\mathcal{H}''(x)/\mathcal{H}(x)$  becomes

$$\frac{1}{\mathcal{H}(x)^2} \frac{d^2\mathcal{H}}{dx^2} = \frac{(1+3w)^2}{2} = \begin{cases} 1, & w = 1/3 \\ 1/4, & w = 0 \\ 1, & w = -1 \end{cases} \quad (29)$$

Equations (28) and (29) offer a means to evaluate the accuracy of our numerical solution at different regimes. Each density parameter evolve differently with  $x$ , as seen from Eqs. (8)-(11). Certain ranges of  $x$ -values will therefore closely resemble a Universe that is dominated by a single fluid. By computing  $\mathcal{H}$ ,  $\mathcal{H}'$ , and  $\mathcal{H}''$ , we can examine whether these quantities exhibit the expected behaviour. This allows us to assess the validity of our model and ensure that it is consistent with the underlying physical principles.

#### 2.2. Implementation details

To solve the differential equations for  $\eta$  and  $t$  (Eq. (14) and (16)) we use the C++ library GSL Galassi (2009), and use their Runge-Kutta4 solver. From the solution we create a spline of the results for the given  $x$  domain we have considered.

We will consider three different ranges of  $x$ -values. For the initial testing, we will use  $x \in [\ln 10^{-10}, 5]$ . For fitting cosmological parameters to the supernova data, we will use  $x \in [\ln 10^{-2}, 0]$ . When we want to estimate important times during the cosmic evolution, we will consider  $x \in [-10, 1]$ , for increased resolution, as the result may vary by a noticeable amount between step sizes. In all cases, we use  $N_x = 10^5$  number of points.

The cosmological parameters we consider assume  $\Omega_{k0} = 0$ . In Sect. 2.2.1 we discuss how we will use supernova data to estimate a value for  $\Omega_{k0}$ . Curvature is therefore implemented in all the relevant methods, but we set  $\Omega_{k0} = 0$  when we're not dealing with supernova fitting.

##### 2.2.1. Supernova fitting and parameter sampling

The supernova data we will use contains  $N = 31$  data points of luminosity distance,  $d_L^{\text{obs}}(z_i)$ , with associated measurement errors,  $\sigma_i$ , at different redshifts,  $z_i \in [0.01, 1.30]$ . This corresponds to  $x \sim [-9.95 \cdot 10^{-3}, -0.833]$ . Using these measurements, we want to constrain the three-dimensional parameter space

$$C = \{\hat{h}, \hat{\Omega}_{m0}, \hat{\Omega}_{k0}\}, \quad (30)$$

where the hat is used to distinguish the estimated parameters from the fiducial ones. We use  $\Omega_{b0} = 0.05$  for this analysis, so  $\hat{\Omega}_{m0}$  enters via  $\Omega_{\text{CDM}0} = \hat{\Omega}_{m0} - \Omega_{b0}$ . Additionally, the neutrinos are not relevant at the small scale considered here, and we therefore set  $N_{\text{eff}} = 0$  for this analysis.

We will assume that the measurements at different redshifts are normal distributed and uncorrelated. The likelihood function is then given by  $L \propto e^{-\chi^2/2}$ , where

$$\chi^2(C) = \sum_{i=1}^N \frac{[d_L(z_i, C) - d_L^{\text{obs}}(z_i)]^2}{\sigma_i^2}, \quad (31)$$

is the function we want to minimize. To do this, we will sample parameter values randomly by a Markov chain Monte Carlo (MCMC) process. We also restrict the parameter space to sample, with the following limits:

$$\begin{aligned} 0.5 < \hat{h} < 1.5, \\ 0 < \hat{\Omega}_{m0} < 1, \\ -1 < \hat{\Omega}_{k0} < 1. \end{aligned} \quad (32)$$

To generate a new sample, we update each parameter by generating a random number  $P \sim \mathcal{N}(0, 1)$ , and multiplying it by a step size. We will use step sizes of  $\Delta\hat{h} = 0.007$ ,  $\Delta\hat{\Omega}_{m0} = 0.05$ ,  $\Delta\hat{\Omega}_{k0} = 0.05$ . To determine whether a new configuration should be included in the sample we use the Metropolis algorithm, where we always accept a state if it yields a lower value of  $\chi^2$  compared to the previous state that was accepted. If the new value of  $\chi^2$  is greater than the old one, we accept it if the ratio of the likelihood functions  $L(\chi_{\text{new}}^2)/L(\chi_{\text{old}}^2) > p$ , where  $p \sim \mathcal{U}(0, 1)$ . We continue drawing samples until we get a total of  $\hat{n} = 10^4$  samples. For the samples generated, we omit the first 1000 samples of the chain from our analysis.

With our generated samples, we can use the best fit,  $\chi_{\text{min}}^2$ , to find the  $1\sigma$  and  $2\sigma$  confidence regions. For the  $\chi^2$  distribution with 3 parameters, these regions are given by  $\chi^2 - \chi_{\text{min}}^2 < 3.53$  and  $\chi^2 - \chi_{\text{min}}^2 < 8.02$ , respectively. We will plot the  $1\sigma$  and  $2\sigma$  constraint in the  $(\Omega_{m0}, \Omega_{\Lambda0})$  plane. Since  $\Omega_{r0} < 10^{-4}$ ,  $\Omega_{\Lambda0}$  can be approximated well by  $\Omega_{\Lambda0} = 1 - \Omega_{m0}$ . After that we will plot the posterior probability distribution function (PDF) for  $H_0$ .

To compare our fit with the Planck data, we will plot  $d_L^{\text{obs}}(z_i)$  together with  $d_L^{\text{fit}}(z)$  and  $d_L^{\text{Planck}}(z)$ . We obtain the former by solving the background cosmology with  $h$ ,  $\Omega_{m0}$ ,  $\Omega_{k0}$  replaced by the configuration  $\hat{h}$ ,  $\hat{\Omega}_{m0}$ ,  $\hat{\Omega}_{k0}$  that yielded the lowest value of  $\chi^2$ .

### 2.3. Results

In this section we present the results from our numerical simulations. Most of our results concern the evolution of various parameters as a function of  $x$ . Whenever it's relevant for interpreting and understanding the plot, we mark the point where we have matter-radiation equality and matter-dark energy equality, corresponding to  $\Omega_m = \Omega_r$  and  $\Omega_m = \Omega_\Lambda$ , respectively. These points can be seen directly in Fig. 5.

#### 2.3.1. Analytical and numerical comparisons

The dimensionless quantity  $\eta\mathcal{H}/c$  is shown in Fig. 1. At the lowest values of  $x \lesssim -10$ , we see that  $\eta\mathcal{H}/c = 1$ , as expected. Slightly before matter-radiation equality takes place, we see a slight increase towards higher  $x$ . As we approach higher  $x$ ,  $\Omega_\Lambda$  starts dominating, and the solution eventually diverges, as expected.



**Fig. 1.** The dimensionless quantity  $\eta\mathcal{H}/c$  as a function of  $x$ . At low  $x$  it has a value of 1, as expected. The most significant changes occur near regions where there is a change in which density parameter is dominating.

In Fig. 2 we have plotted  $\mathcal{H}'/\mathcal{H}$  and  $\mathcal{H}''/\mathcal{H}$ , where we include the analytical approximation from Eq. (28) and Eq. (29), respectively. The different values of  $w$  are drawn over the whole range of  $x$  where their related density parameter is larger than the other two. This is done for visibility purposes, and we only expect approximations to be reasonable whenever a density parameter is close to 1.

Towards the smallest values of  $x$  we see that both quantities are well approximated by the analytical solutions for  $w = 1/3$ . As we reach  $x \gtrsim 12$ , matter becomes increasingly dominant, and the solution deviates from being purely dominated by a  $w = 1/3$  fluid. Towards the highest values of  $x$ , we see that both quantities reach a constant value of 1 for  $w = -1$ . At higher values of  $x$ , we know that both  $\Omega_m(x)$  and  $\Omega_r(x)$  should vanish, eventually, while  $\Omega_\Lambda \rightarrow 1$ . This behaviour is thus present in our implementation. When matter dominates, we see that both functions exhibit inferior agreement with the approximations compared to the other regimes. This can be understood from Fig. 5, where the vanishing contribution of  $\Omega_r$  occurs around the same time as  $\Omega_\Lambda$  starts contributing. The maximum value reached for this particular configuration is  $\Omega_m \approx 0.995$ . Nonetheless, significant deviations from the analytical solutions are not evident.



**Fig. 2.**  $\mathcal{H}'/\mathcal{H}$  and  $\mathcal{H}''/\mathcal{H}$  compared with analytical expressions in the case a single fluid with a given EoS parameter,  $w$ , shown by the dashed lines. The transition between the dashed lines are chosen as the corresponding epochs of equality.

#### 2.3.2. Hubble factor and time variables

Having checked that our implementation is physical, we now proceed by studying the evolution of the background, starting with a plot of the conformal Hubble factor,  $\mathcal{H}(x)$ , shown in Fig. 3.

The local minima taking place before matter-dark energy equality corresponds to the onset of acceleration, where  $\ddot{a} = 0$ . For  $x > 0$ ,  $\Omega_\Lambda$  will dominate the conformal Hubble factor, where we have  $\mathcal{H}(x) \propto e^x$ , as seen from Eq. (7).



**Fig. 3.** Evolution of the conformal Hubble factor. The minimum point marks the onset of acceleration, after which, dark energy dominates its evolution.

The evolution of  $\eta(x)$  and  $t(x)$  is shown in Fig. 4. At high values of  $x$ , the  $e^x$  dependence of  $\mathcal{H}(x)$  causes  $\eta(x)$  to grow as  $e^{-x}$  at late times, suppressing its growth. The cosmic time, on the other hand, does not have an exponential dependence in the integrand at high values of  $x$ . This yields the linear growth we see at late times. The different  $x$ -dependence of  $t$  and  $\eta$  results in the two quantities to be approximately equal at  $x \sim 2.75$ .



**Fig. 4.** The cosmic time,  $t$  and conformal time  $\eta/c$ . We emphasize that  $\eta \neq t$  at small  $x$ , but the difference is discernable on the scale considered.



**Fig. 5.** Evolution of the density parameters over time. The points where  $\Omega_m = \Omega_r$  marks the epoch of matter-radiation equality, and the intersection between  $\Omega_m$  and  $\Omega_\Lambda$  marks the epoch of matter-dark energy equality. The sum of the three quantities never exceed 1, as expected.

### 2.3.3. Supernova fitting

A plot showing the luminosity distance as a function of redshift is shown in Fig. 6, where we plot  $d_L(z)/z$  to better compare the simulations with the data. There is a noticeable discrepancy between the simulated luminosity distance and the data, with most redshifts causing the simulation to fall outside the uncertainties.

The  $1\sigma$  and  $2\sigma$  confidence regions in the  $\Omega_\Lambda - \Omega_m$  plane is shown in Fig. 7. In the figure we have also indicated the parameter configuration for a flat Universe. A majority of the configurations seem to favour a non-flat Universe, with  $\Omega_{k0} \approx 0.0674$ . This could be a result of local variations in the gravitational field at small scales.

The posterior PDF of  $H_0$  is shown in Fig. 8, where we have included the resulting Gaussian distribution from the mean and variance of the sampled  $H_0$  values. This shows further discrepancy from the value of  $H_0 = 67$  km/s/Mpc, given by Planck, while the mean value we obtain is  $\bar{H}_0 = 70.1$  km/s/Mpc, with a corresponding standard deviation of  $\sigma_{H_0} = 0.64$  km/s/Mpc.



**Fig. 6.** Supernova data compared with the predicted luminosity distance obtained from simulations using Planck cosmology. Note that we use a logarithmic scale for the y-axis.

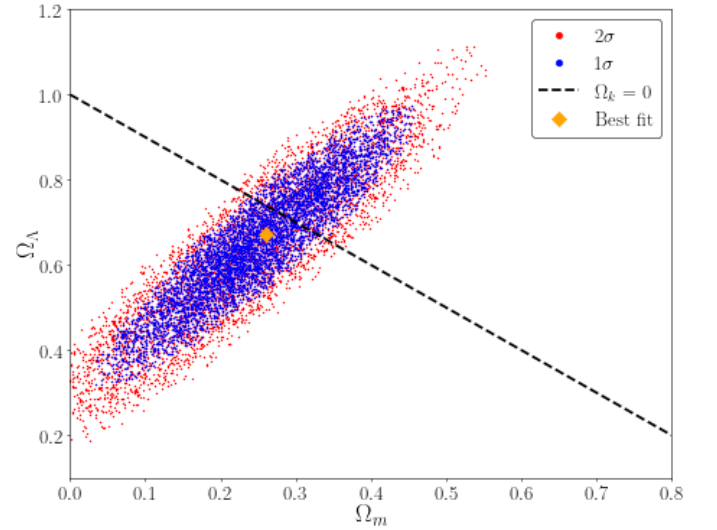


**Fig. 7.** Confidence regions of  $\Omega_{m0}$  and  $\Omega_{\Lambda0}$  obtained from fitting the supernova data. The best fit parameter values are shown in the plot, as well as the configurations that would give a flat Universe.

With the fitted parameters, we can solve the background cosmology once again, and compute the resulting luminosity distance. The result is shown in Fig. 9, where the previous result from Fig. 6 is included for comparison purposes. The simulation with the best fit parameters yields a luminosity distance function that is much more consistent with data. However, there is still some discrepancy at lower redshift, but the associated data points in this regime have large uncertainties.

There are three important periods we have discussed, the times of matter-radiation equality, acceleration onset and matter-dark energy equality. The times when these incidents occur are listed in table 2.3.3, in terms of  $x$ , redshift  $z$  and cosmic time  $t$ . We also include the age of the Universe today,  $t_0 \equiv t(x = 0)$ , and the conformal time today,  $\eta_0/c$ .

	Matter-radiation equality $\Omega_m = \Omega_r$	Acceleration onset $\ddot{a} = 0$	Matter-dark energy equality $\Omega_m = \Omega_\Lambda$
$x$	-8.132	-0.487	-0.256
$z$	3400.460	0.627	0.291
$t$ [Gyr]	$5.099 \cdot 10^{-5}$	7.750	10.372

Age of Universe today:  $t_0 = 13.848$  Gyr

Conformal time today:  $\eta_0/c = 46.284$  Gyr

**Table 1.** Important times during the evolution of the Universe, expressed in terms of  $x$ , redshift and cosmic time. In the last two rows we also present today's time values



**Fig. 8.** Posterior PDF of  $H_0$ . The histogram shows the sampled values, while the blue curve is the corresponding normal distribution obtained from the mean and variance of the data.



**Fig. 9.** The luminosity distance function obtained from the best fit values of  $C$  (blue line), compared with the result from the Planck cosmology (dashed green line), which is also shown in Fig. 6.

### 3. Milestone II

Having successfully implemented the background cosmology, the next step in developing our model is to include interactions between particles. After the Big Bang, the early universe was highly ionized. Due to Thompson scattering, photons were strongly coupled to baryons. As the Universe expanded, and the temperature dropped, neutral atoms were able to form, and the photons were able to escape from the plasma. These are the CMB photons we observe today. The period where neutral atoms formed is called recombination, and will be the main topic of this section. Our goal is to compute the number density of free electrons in the Universe, and use this to estimate when recombination occurred. The evolution of free electrons will affect both structure formation and the resulting power spectrum of the CMB photons, as we will study later.

We will use both the Saha and Peebles equation to compute the electron number density, and use this to compute the optical depth. From the optical depth, we will compute the so-called *visibility function*. In this section we will adapt natural units, where we set  $c = \hbar = k_B = 1$ . Additionally, we will make the assumption that Hydrogen is the only element present in the universe. Hence, we use  $Y_p = 0$ , rather than the value from Planck, given in Eq. (A.1), as we neglect Helium and heavier elements.

#### 3.1. Theory

##### 3.1.1. Optical depth and visibility function

A source that emits light with an intensity  $I_0$  is attenuated by a factor  $e^{-\tau(x)}$  as it travels through a medium, where  $\tau$  is the optical depth of the medium. In the early universe we have  $\tau \gg 1$ , and the universe is said to be optically thick. As the universe expands and recombination takes place, the universe becomes optically thin,  $\tau \ll 1$ , and light is able to escape the primordial plasma and reach us. Considering Thompson scattering only, the optical depth is defined in terms of the scale factor,  $a$ , as (Callin 2006, Eq. (5))

$$\tau(\eta) = \int_{\eta}^{\eta_0} d\eta' n_e \sigma_T a, \quad (33)$$

where  $n_e$  is the number density of free electrons,

$$\sigma_T = \frac{8\pi\alpha^2}{3m_e^2} = 6.6524587158 \cdot 10^{-29} \text{ m}^2 \quad (34)$$

is the Thompson cross-section and  $a$  is the scale factor.  $\alpha$  is the fine-structure constant and  $m_e$  is the electron mass. Using Eq.

(14), we can rewrite Eq. (33) as a differential equation

$$\frac{d\tau}{dx} = -\frac{n_e \sigma_T}{H}, \quad (35)$$

which we can solve numerically once we know  $n_e$ . The initial condition is  $\tau(x=0) = 0$ , as the universe is transparent today.

From the optical depth, we obtain the so-called *visibility function* (Callin 2006, Eq. (8))

$$\tilde{g}(x) = -\tau' e^{-\tau}, \quad (36)$$

which is normalized as

$$\int_{-\infty}^0 dx \tilde{g}(x) = 1. \quad (37)$$

The normalization means that  $\tilde{g}(x)$  is a probability distribution, and we may interpret it as the probability of an observed CMB photon today having experienced its last scattering at a time  $x$ . The visibility function is sharply peaked around the time when the photons decouple from the baryons, and is often referred to as the surface of last scattering. We may therefore use the peak of  $\tilde{g}(x)$  to estimate the time when decoupling took place in the early universe.

### 3.1.2. Electron density

The final thing we need to compute  $\tau$  and  $\tilde{g}$  is the number density of free electrons. To compute the evolution of free electrons, we have to consider the Boltzmann equation (Dodelson 2020, Eq. (3.19))

$$\frac{df}{dt} = C[f], \quad (38)$$

where  $f$  is the distribution function and  $C[f]$  is a collision term.

We will not consider the full Boltzmann equation, but an approximated version relevant for the recombination. Following the notation and definitions from (Dodelson 2020, Eq. (4.5)-(4.9)), the equation we consider is given as

$$a^{-3} \frac{d(n_i a^3)}{dt} = n_i^{(0)} n_2^{(0)} \langle \sigma v \rangle \left\{ \frac{n_3 n_4}{n_3^{(0)} n_4^{(0)}} - \frac{n_1 n_2}{n_1^{(0)} n_2^{(0)}} \right\}, \quad (39)$$

where  $n_i$  denotes the number density of a particle species  $i$ , with  $n_i^{(0)}$  referring to its value in chemical equilibrium, and  $\langle \sigma v \rangle$  is the thermally averaged cross-section. The only reaction we will consider for recombination is

$$e^- + p^+ \leftrightarrow H + \gamma. \quad (40)$$

For the photons we will assume  $n_\gamma = n_\gamma^{(0)}$ . From now on we use  $e$  and  $p$  as subscripts to denote free electrons and protons, respectively, and a subscript  $H$  to denote neutral Hydrogen.

Instead of computing  $n_e$  directly, we will compute the fractional electron density

$$X_e \equiv \frac{n_e}{n_e + n_H} \approx \frac{n_e}{n_b}, \quad (41)$$

where  $n_b$  is the total baryon density of the universe. Since the universe must be electrically neutral, we have  $n_e = n_p$ , and assuming no heavier elements than Hydrogen gives  $n_b \approx n_p + n_H$ . Neglecting the small mass difference between the proton and the Hydrogen, the baryon density can be written as

$$n_b \approx \frac{\rho_b}{m_H} = \frac{\Omega_{b0} \rho_{c0}}{m_H a^3}, \quad (42)$$

where  $\rho_{c0} \equiv \frac{H_0^2}{8\pi G}$  is the critical density of the universe today and  $m_H$  is the Hydrogen mass.

Before recombination occurs, the interaction rates greatly exceed the expansion rate of the universe, and for Eq. (39) to be valid we must have that

$$\frac{n_e n_p}{n_H} = \frac{n_e^{(0)} n_p^{(0)}}{n_H^{(0)}}. \quad (43)$$

In terms of  $X_e$ , this reduces to the Saha equation

$$\frac{X_e^2}{1 - X_e} = \frac{1}{n_b} \left( \frac{m_e T_b}{2\pi} \right)^{3/2} e^{-\epsilon_0/T_b}, \quad (44)$$

where  $T_b$  is the temperature of the baryons, and  $\epsilon_0$  is the Hydrogen ionization energy. The time evolution of  $T_b$  is governed by a differential equation coupled to  $X_e$ . However, we will assume that it follows the photon temperature,  $T_\gamma$ , evolving as

$$T_b = T_\gamma = T_{\text{CMB}0} e^{-x}. \quad (45)$$

At later times, Eq. (43) is no longer a valid approximation, and we have to solve Eq. (39). Additionally, we have to take processes related to atomic physics into account, so the differential equation we will consider is the Peebles equation

$$\frac{dX_e}{dx} = \frac{C_r(T_b)}{H} [\beta(T_b)(1 - X_e) - n_H \alpha^{(2)}(T_b) X_e^2], \quad (46)$$

where  $C_r(T_b)$ ,  $\beta(T_b)$  and  $\alpha^{(2)}(T_b)$  are quantities related to interaction effects, and are given by

$$C_r(T_b) = \frac{\Lambda_{2s \rightarrow 1s} + \Lambda_\alpha}{\Lambda_{2s \rightarrow 1s} + \Lambda_\alpha + \beta^{(2)}(T_b)}, \quad (47a)$$

$$\Lambda_{2s \rightarrow 1s} = 8.227 \text{ s}^{-1}, \quad (47b)$$

$$\Lambda_\alpha = H \frac{(3\epsilon_0)^3}{(8\pi)^2 n_{1s}}, \quad (47c)$$

$$n_{1s} = (1 - X_e) n_H, \quad (47d)$$

$$\beta^{(2)}(T_b) = \beta(T_b) e^{3\epsilon_0/4T_b}, \quad (47e)$$

$$\beta(T_b) = \alpha^{(2)}(T_b) \left( \frac{m_e T_b}{2\pi} \right)^{3/2} e^{-\epsilon_0/T_b}, \quad (47f)$$

$$\alpha^{(2)} = \frac{64\pi}{\sqrt{27}\pi} \frac{\alpha^2}{m_e^2} \sqrt{\frac{\epsilon_0}{T_b}} \phi_2(T_b), \quad (47g)$$

$$\phi_2(T_b) = 0.448 \ln(\epsilon_0/T_b). \quad (47h)$$

The main reason behind these additional equations is that Hydrogen production is inefficient at  $T_b \approx \epsilon_0$ . Direct recombination to the Hydrogen ground state is likely to produce a photon with energy greater than  $\epsilon_0$ , which will ionize another nearby Hydrogen atom, resulting in no net Hydrogen production. Recombination is achieved when an electron and proton combine to an excited Hydrogen atom, followed by the atom's decay into the ground state, which is a slow process.

In Sect. 3.2.2 we discuss how combine the Saha and Peebles equation to compute  $X_e$ .

### 3.1.3. Sound Horizon at decoupling

Before recombination happens, baryons and photons are tightly coupled. For this reason, the baryons and photons behave as if

they were a single fluid, and the sound speed of this fluid is given by (Dodelson 2020, Eq. (9.21)) (where we use  $R \rightarrow 1/R$ )

$$c_s(x) = \frac{c}{\sqrt{3}} \sqrt{\frac{R(x)}{1+R(x)}}, \quad R(x) = \frac{4\Omega_\gamma(x)}{3\Omega_b(x)}. \quad (48)$$

The total co-moving distance a sound wave in this plasma could have travelled since the Big Bang is known as the sound-horizon, which is given as

$$s(x) = \int_{-\infty}^x \frac{dx' c_s}{\mathcal{H}}. \quad (49)$$

From this we can compute the sound horizon at decoupling,  $r_s = s(x_{\text{rec}})$ , which is an important quantity of the CMB. Thus, we have an additional ODE to solve,

$$\frac{ds(x)}{dx} = \frac{c_s}{\mathcal{H}}, \quad (50)$$

with  $s(x_{\text{ini}}) = \frac{c_s(x_{\text{ini}})}{\mathcal{H}(x_{\text{ini}})}$  as the initial condition, following the same reasoning as we did for  $\eta'(x)$  in Eq. (15).

### 3.2. Implementation details

To compute  $X_e$ , we use the Saha equation initially, as it is a good approximation at early times when  $X_e \approx 1$ . This is also the regime where the Peebles equation is unstable, and we therefore consider the Saha equation for  $X_e > X_e^{\text{tol}}$ . Once we reach  $X_e < X_e^{\text{tol}}$  we use the final value from the Saha equation as our initial condition to solve the Peebles equation. The Peebles equation is then used all the way to today, at  $x = 0$ . For this report, we choose  $X_e^{\text{tol}} = 0.99$ . For comparison with the Saha equation alone, we set  $X_e^{\text{tol}} = 10^{-6}$ . Once  $X_e$  is computed we get  $n_e(x)$  from Eq. (41).

#### 3.2.1. Solving the Saha Equation

Solving the Saha equation is done by solving a quadratic formula for  $X_e$ . At early times, however, the RHS of Eq. (44) will be enormous, and may cause numerical errors when solving the quadratic formula. To avoid this, we use the first order approximation  $\sqrt{1+x} \approx 1 + \frac{x}{2}$  for  $|x| \ll 1$  at early times. The Saha equation is thus implemented as

$$X_e = \begin{cases} 1, & y > 10^7, \\ \frac{y}{2} \left[ -1 + \sqrt{1 + 4/y} \right], & y \leq 10^7, \end{cases} \quad (51)$$

where  $y$  refers to the RHS of Eq. (44). Since  $X_e$  is strictly positive, we have omitted the negative solution. The exact value of  $10^7$  is chosen to ensure both  $X_e \not\approx 1$ , and  $X_e \not\ll X_e^{\text{tol}}$  when the quadratic formula is to be used.

#### 3.2.2. Solving the Peebles Equation

To solve Eq. (46) numerically, we follow the same procedure as we did for  $\eta(x)$ , but for the initial condition we use the final value of  $X_e$  that we obtained from the Saha equation.

At late times, when the baryon temperature gets low, the exponential term in Eq. (47e) for  $\beta^{(2)}(T_b)$  become sufficiently large to yield an overflow. However, this is also where  $\beta(T_b) \rightarrow 0$ , due to its exponential factor (Eq. (47f)). This exponential factor causes  $\beta^{(2)}(T_b) \rightarrow 0$  at late times. To avoid overflow, we implement the equation for  $\beta^{(2)}(T_b)$  as

$$\beta^{(2)}(T_b) = \begin{cases} 0, & \epsilon_0/T_b > 200, \\ \beta(T_b)e^{3\epsilon_0/4T_b}, & \epsilon_0/T_b \leq 200. \end{cases} \quad (52)$$

#### 3.2.3. Optical depth and visibility function

With  $n_e$  we can then solve Eq. (35) for  $\tau(x)$  with the aforementioned initial condition of  $\tau(x=0) = 0$ . We therefore integrate backwards, starting from  $x = 0$ . The visibility function is now easily obtained, as  $\tau'(x)$  is given analytically by Eq. (35). From this, we get immediately  $\tilde{g}(x)$ .

We also need the second derivative of  $\tau$ , as well as the first two derivatives of  $\tilde{g}$ . For  $\tau''(x)$ , we compute it from numerically differentiating the  $\tau'(x)$  data.<sup>1</sup> We use this to compute

$$\tilde{g}'(x) = (\tau'(x)^2 - \tau''(x))e^{-\tau(x)}, \quad (53)$$

and obtain  $\tilde{g}''(x)$  by numerically differentiating  $\tilde{g}'(x)$ . This is done to avoid potential errors that may occur when numerically computing the second derivative of  $\tilde{g}(x)$ , if  $\tilde{g}(x)$  is somewhat ill-behaved at certain times.<sup>2</sup>

#### 3.2.4. Determining the time of recombination and decoupling

To estimate the times when recombination takes place, we define this as

$$X_e(x = x_{\text{recombination}}) = 0.1, \quad (54)$$

where the value  $X_e = 0.1$  is chosen arbitrarily.

For decoupling, we find  $x_{\text{decoupling}}$  as the point where  $\tilde{g}'(x_{\text{decoupling}}) = 0$ . However, we limit the time values to  $x \in [x_0 \pm 0.1]$ , where  $x_0$  is defined by  $\tau(x_0) = 1$ . This is done to avoid  $x$  values where  $\tilde{g}(x) = 0$ .

### 3.3. Results

#### 3.3.1. Electron fraction

The evolution of the electron fraction with time is shown in Fig. 10. Here, we have included the solution obtained through the Saha equation alone for comparison. In the figure we also show the time periods when recombination occurs according to the two solutions, i.e. when  $X_e = 0.1$ . The time of decoupling has been omitted, since it is very close to the recombination time, as shown in table 2.

We see that the Peebles equation predicts the production of neutral Hydrogen to take much longer time than the Saha equation. Recombination therefore occurs at a much lower temperature than the binding energy of Hydrogen, as expected. Towards  $x = 0$  the Peebles equation give  $X_e \ll 1$ , but we never reach  $X_e = 0$  entirely. From our solution we find that the current value is  $X_e(x=0) \approx 2.026 \cdot 10^{-4}$ . On the other hand, the Saha equation reaches  $X_e = 0$  before  $x = 0$  is reached, predicting now free electrons in the universe.

#### 3.3.2. Optical depth and visibility function

The optical depth, and its first two derivatives is shown in Fig. 11. We see that the three quantities rapidly drop by several orders of magnitude near  $x = -7$ , around the time of recombination. Looking at Fig. 12 we see that the rapidly varying optical depth results in a sharply peaked  $\tilde{g}$ .

<sup>1</sup> Couldn't we just compute it analytically? I get a tiny "bump" in  $\tau''$  near  $X_e^{\text{tol}}$ , and I don't know if this will cause problems later on, and therefore didn't want to spend too much time on it if wasn't needed.

<sup>2</sup> I don't know if this is useful, or helps, at all. I don't know if we care about the derivatives at  $x$ -values where this might be an issue.



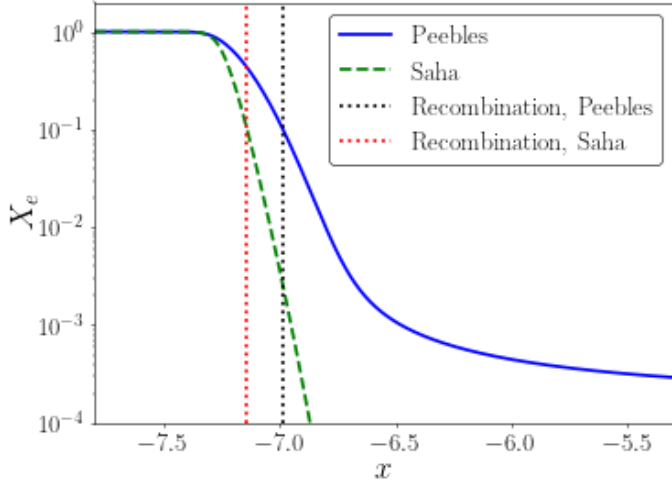


**Fig. 10.** Free electron fraction computed from the Saha equation only (dashed green curve) and from the Peebles equation (solid blue curve), where the Saha equation was used at early times, until  $X_e < 0.99$ . The recombination times is shown for both solutions.

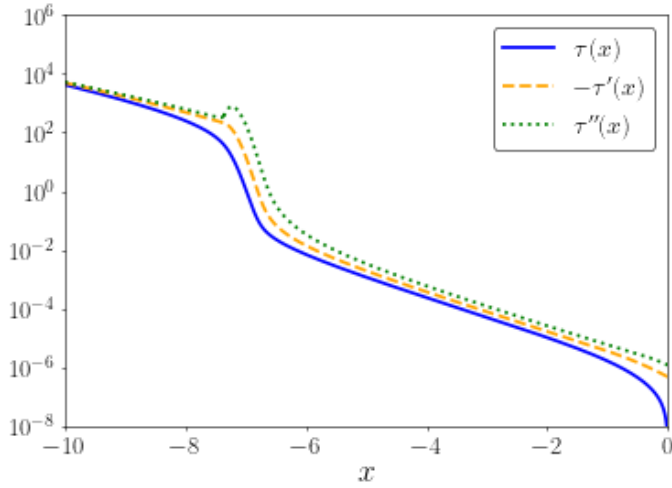


**Fig. 11.** The optical depth,  $\tau(x)$  and its two first derivatives with respect to  $x$ .

### 3.3.3. Times of recombination and decoupling

The period of recombination and decoupling, as computed from the Peebles equation, is given in table 2. We see that the photons and baryons decouple later than recombination occurs, as is expected. This does depend on how we define the two periods, and is thus not a very conclusive result on its own. Using a higher value of  $X_e$  for instance would yield a larger separation between the two events.

**Table 2.** Times when decoupling and recombination occurs, computed from the Peebles equation.

Peebles	$x$	$z$	$t$ [yr]	$r_s$ [Mpc]
Decoupling	-6.98534	1079.7	377 782	145.3
Recombination	-6.98549	1079.8	377 690	

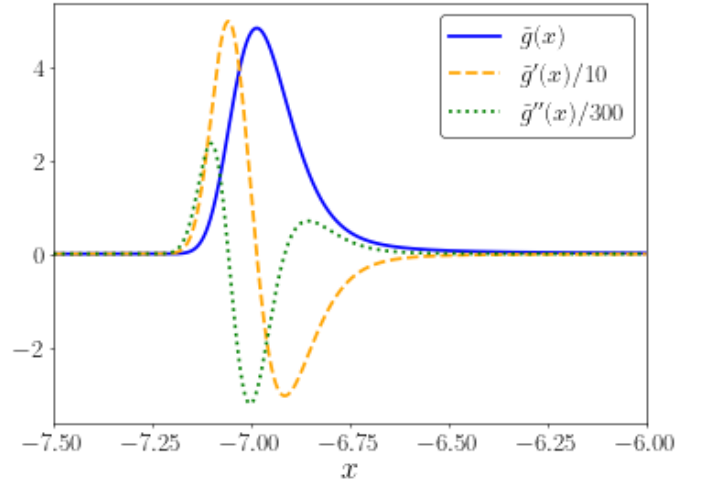


**Fig. 12.** The visibility function,  $\tilde{g}(x)$  (solid curve), and its derivatives,  $\tilde{g}'(x)/10$  (dashed curve) and  $\tilde{g}''(x)/300$  (dotted curve). The derivatives have been scaled in order to view them all in the same plot.

**Table 3.** Times when decoupling and recombination occurs, computed from the Saha equation.

Saha	$x$	$z$	$t$ [yr]
Decoupling	-7.15485	1279.3	283 611
Recombination	-7.14035	1260.9	290 686

## 4. Milestone III

So far we have only considered the flat FLRW metric for a homogeneous Universe, and used this to study the recombination history of the Universe. In this section we will consider small perturbations to the background, and thereby introduce inhomogeneities. We will consider perturbations to the FLRW metric and the matter contents of the Universe, where we limit ourselves to photons, baryons and CDM. We will restrict ourselves to linear perturbations only, which allows us to derive good approximations for the Boltzmann and Einstein equations. From this we are able to study the evolution of structure in the early Universe, which we later will connect to statistical observables in the Universe. This means that we ignore contributions from neutrinos and polarization. This means that we set  $\mathcal{N}_{\text{eff}} = 0$  when we compute relevant quantities from Sect. 2 and Sect. 3 that we will need in this section.

If you encounter red text in this section and/or low-resolution PNG figures, it means that this version is not complete (as is obvious from the text).

### 4.1. Theory

In this section we present the equations governing the evolution of the perturbed quantities. We will only present the relevant equations here, which are all obtained from Dodelson (2020) and Callin (2006), unless otherwise stated. We refer to Dodelson for a detailed derivation of the equations. For the notation, we adapt that of Callin. Throughout this section, we will consider perturbations in Fourier space.

#### 4.1.1. Perturbation quantities

For the perturbed metric we consider the Newtonian gauge, and write it as

$$g_{\mu\nu} = \begin{pmatrix} -(1+2\Psi) & 0 \\ 0 & a^2\delta_{ij}(1+2\Phi) \end{pmatrix}, \quad (55)$$

where we have introduced the scalar perturbations  $\Psi$  and  $\Phi$ , which are functions of both position and time. For  $\Psi = \Phi = 0$  we obtain the FLRW metric. Photon perturbations are defined in terms of the relative temperature variations,  $\Theta \equiv \delta T/T$ , via

$$T(\mathbf{k}, \mu, \eta) = T^{(0)}(\eta) [1 + \Theta(\mathbf{k}, \mu, \eta)], \quad (56)$$

where  $\mathbf{k}$  is the Fourier transformed variable corresponding to position  $\mathbf{x}$ , and  $\mu \equiv \frac{\mathbf{k} \cdot \mathbf{p}}{kp}$ . The temperature perturbations only depend on the photon momentum in terms of their directions, and we therefore expand  $\Theta$  in terms of multipoles as

$$\Theta_\ell = \frac{i^\ell}{2} \int_{-1}^1 \mathcal{P}_\ell(\mu) \Theta(\mu) d\mu \Leftrightarrow \Theta(\mu) = \sum_{\ell=0}^{\infty} \frac{2\ell+1}{i^\ell} \Theta_\ell \mathcal{P}_\ell(\mu), \quad (57)$$

where  $\mathcal{P}_\ell(\mu)$  are Legendre polynomials. The first three multipoles are the monopole,  $\Theta_0$ , the dipole,  $\Theta_1$  and the quadrupole,  $\Theta_2$ . The monopole represents the background temperature of the CMB and the dipole represents our relative velocity with respect to the CMB.

We denote density perturbations of CDM and baryons as  $\delta_{\text{CDM}}$  and  $\delta_b$ , and their velocity perturbations as  $v_{\text{CDM}}$  and  $v_b$ . From the perturbed Einstein equations one can show that  $\delta_\gamma = 4\Theta_0$  and  $v_\gamma = -3\Theta_1$  for the photons.

#### 4.1.2. Perturbation equations

The system of ODEs we will solve for the evolution of the perturbed quantities are given in (Callin 2006, Eq. (22)), where we neglect neutrinos and polarization and set  $\Theta_P = \mathcal{N} = 0$ .

$$\Theta'_0 = -\frac{k}{\mathcal{H}} \Theta_1 - \Phi', \quad (58a)$$

$$\Theta'_1 = \frac{k}{3\mathcal{H}} \Theta_0 - \frac{2k}{3\mathcal{H}} \Theta_2 + \frac{k}{3\mathcal{H}} \Psi + \tau' \left[ \Theta_1 + \frac{1}{3} v_b \right], \quad (58b)$$

$$\Theta'_\ell = \frac{\ell k}{(2\ell+1)\mathcal{H}} \Theta_{\ell-1} - \frac{(\ell+1)k}{(2\ell+1)\mathcal{H}} \Theta_{\ell+1} + \tau' \left[ \Theta_\ell - \frac{1}{10} \Pi \delta_{\ell,2} \right], \quad 2 \leq \ell < \ell_{\text{max}}, \quad (58c)$$

$$\Theta'_\ell = \frac{k}{\mathcal{H}} \Theta_{\ell-1} - c \frac{(\ell+1)}{\mathcal{H}\eta(x)} \Theta_\ell + \tau' \Theta_\ell, \quad \ell = \ell_{\text{max}}, \quad (58d)$$

$$\delta'_{\text{CDM}} = \frac{k}{\mathcal{H}} v_{\text{CDM}} - 3\Phi', \quad (58e)$$

$$v'_{\text{CDM}} = -v_{\text{CDM}} \frac{k}{\mathcal{H}} \Psi, \quad (58f)$$

$$\delta'_b = \frac{k}{\mathcal{H}} v_b - 3\Phi', \quad (58g)$$

$$v'_b = -v_b - \frac{k}{\mathcal{H}} \Psi + \tau' R(3\Theta_1 + v_b), \quad (58h)$$

$$\Phi' = -\Psi - \frac{k^2}{3\mathcal{H}^2} \Phi + \frac{H_0^2}{2\mathcal{H}^2} [\Omega_{\text{CDM}0} a^{-1} \delta_{\text{CDM}} + \Omega_{b0} a^{-1} \delta_b + 4\Omega_{\gamma0} a^{-2} \Theta_0], \quad (58i)$$

$$\Psi = -\Phi - \frac{12H_0^2}{k^2 a^2} \Omega_{\gamma0} \Theta_2. \quad (58j)$$

We have  $\Pi = \Theta_2$  due to  $\Theta_P = 0$ , and have written  $\Pi$  for clarity.

The expression for  $\Theta'_\ell$  is recursive, and we thus need to truncate the series at some point. Truncating the series by setting  $\Theta_{\ell_{\text{max}}} = 0$  would lead to numerical errors propagating down to  $\Theta_2$ . Eq. (58d) comes from assuming  $\Theta_\ell(k, \eta) \sim j_\ell(k\eta)$  at high  $\ell$ , where  $j_\ell(k\eta)$  is the spherical Bessel function, and using the recurrence relation for  $j_\ell$  (see Callin 2006, Eq. (46)-(49)).

The equation for  $\Psi$  is an algebraic equation, and its value is inserted in the other equations. Noting that  $\Phi'$  is the only derivative of a perturbed quantity found on the RHS of Eqs. (58), we solve for it first, and insert this value into the other equations.

At early times, photons and electrons are tightly coupled, and  $\tau$  is therefore very high. In this regime, Eq. (58) becomes numerically unstable, so we have to resort to approximations, which we discuss in the next section.

#### 4.1.3. Initial conditions

We will use adiabatic initial conditions, and follow the convention used by Winther (2023), with  $f_\nu = 0$  as we omit neutrinos<sup>3</sup>. The set of ODEs we solve are linear, so we can choose a particular normalization, which we adjust for when computing the Power spectrum later on. The initial conditions are

$$\Psi = -\frac{2}{3}, \quad (59a)$$

$$\Phi = -\Psi, \quad (59b)$$

$$\delta_{\text{CDM}} = \delta_b = -\frac{3}{2} \Psi, \quad (59c)$$

$$v_{\text{CDM}} = v_b = -\frac{k}{2\mathcal{H}} \Psi, \quad (59d)$$

$$\Theta_0 = -\frac{1}{2} \Psi, \quad (59e)$$

$$\Theta_1 = \frac{k}{6\mathcal{H}} \Psi. \quad (59f)$$

Initially,  $\tau$  is very large, so photons and baryons behave as a single fluid, and is referred to as the *Tight coupling regime*. This implies that temperature gradients are washed out, as the system is in thermodynamic equilibrium. Since  $\tau'$  is large at early times, it means that the terms proportional to  $\tau'$  in Eq. (58) can be neglected. This implies that  $\Theta_\ell = 0$  for  $\ell \geq 2$ . However, we need the lowest non-zero contribution from these multipoles when numerically integrating the system of ODEs. By expanding in terms of  $k/\mathcal{H}\tau' \ll 1$  and using the initial conditions, one can obtain the following expression for the higher order multipoles

$$\Theta_2 = -\frac{20k}{45\mathcal{H}\tau'} \Theta_1, \quad (60a)$$

$$\Theta_\ell = -\frac{\ell}{2\ell+1} \frac{k}{\mathcal{H}\tau'} \Theta_{\ell-1}. \quad (60b)$$

These are the expressions we will use to compute the multipoles during tight coupling. Note that we  $\Theta_1 \simeq -v_b/3$  in this regime. To avoid numerical instability when multiplying this with  $\tau'$  in Eq. (58b) we derive a modified expression for  $\Theta'_1$  and  $v'_b$  in Sect. 4.2.1. Furthermore, we discuss in that section how we determine when to stop using the tight coupling approximation.

<sup>3</sup> Note that Winther has a sign error in his expression for the initial condition for  $\Psi$

#### 4.1.4. Line-of-sight integration

From Eq. (58c) we see that we have to solve a huge system of ODEs if we want to probe the CMB to scales around  $\ell \sim 1000$ . However, by exploiting the LOS-integration technique Seljak & Zaldarriaga (1996),  $\Theta_\ell$  can be obtained from computing the integral

$$\Theta_\ell(k, x=0) = \int_{-\infty}^0 \tilde{S}(k, x) j_\ell[k(\eta_0 - \eta(x))] dx, \quad (61)$$

where  $\tilde{S}(k, x)$  is the source function, which is given by

$$\begin{aligned} \tilde{S}(k, x) = & \tilde{g} \left[ \Theta_0 + \Psi + \frac{1}{4}\Pi \right] + e^{-\tau} [\Psi' - \Phi'] \\ & - \frac{1}{k} \frac{d}{dx} (\mathcal{H} \tilde{g} v_b) + \frac{3}{4k^2} \frac{d}{dx} \left[ \mathcal{H} \frac{d}{dx} (\mathcal{H} \tilde{g} \Pi) \right]. \end{aligned} \quad (62)$$

Since we have  $\Pi = \Theta_2$ , the highest photon multipole required to compute any multipole  $\Theta_\ell$  from Eq. (61) is  $\Theta_2$ . Thus, the number of multipoles we have to compute from the coupled ODEs in Eq. (58) is governed by the value of  $\ell_{\max}$  which ensures sufficient accuracy in  $\Theta_2$ .

**explain terms**

#### 4.1.5. Evolution of different modes

Eq. (58) governs the evolution of a single mode. As the horizon grows, causal physics will affect perturbations on increasingly larger scales. Initially,  $k\eta \ll 1$ , and all modes are outside the horizon, and as  $\eta$  grows, more and more modes will enter the horizon. To study the evolution of perturbations, we therefore consider three different modes. We choose one short wavelength mode that enter the horizon at early times, one large wavelength mode entering the horizon at late times, and one mode of intermediate scale. Which epoch the Universe is in when a mode enters the horizon affects the evolution of the mode.

Defining  $x_{\text{entry}}$  as  $k\eta(x_{\text{entry}}) = 1$ , we choose three different values of  $k$

$$\begin{aligned} k \in \{0.001, 0.03, 0.3\}/\text{Mpc}, \\ x_{\text{enter}} \in \{-5.182, -9.726, -12.098\}, \end{aligned} \quad (63)$$

where the first and last element of  $x_{\text{enter}}$  correspond to modes entering the horizon when  $\Omega_m \approx 0.95$  and  $\Omega_\gamma \approx 0.95$ , respectively. The intermediate mode will enter when  $\Omega_m \approx 0.25$  and  $\Omega_\gamma \approx 0.25$ . The long wavelength mode will enter the horizon long after recombination has taken place, compared to the other two modes, which enters prior to recombination. This allows us to compare the effect recombination has on the evolution of the perturbations. We postpone the details regarding evolution of these modes to Sect. 4.3.

#### 4.2. Implementation details

##### 4.2.1. Tight coupling regime

During tight coupling, Eq. (64c) needs to be modified to avoid numerically instability at early times. Following Callin, the tight

coupling regime is computed with

$$\begin{aligned} \varrho q = & -[(1-R)\tau' + (1+R)\tau''](3\Theta_1 + v_b) \\ & - \frac{k}{\mathcal{H}} \Psi + (1 - \frac{\mathcal{H}'}{\mathcal{H}}) \frac{k}{\mathcal{H}} (-\Theta_0 + 2\Theta_2) - \frac{k}{\mathcal{H}} \Theta_0', \end{aligned} \quad (64a)$$

$$v_b' = \frac{1}{1+R} \left[ -v_b - \frac{k}{\mathcal{H}} \Psi + R(q + \frac{k}{\mathcal{H}} [-\Theta_0 + 2\Theta_2 - \Psi]) \right], \quad (64b)$$

$$\Theta_1' = \frac{1}{3}(q - v_b'), \quad (64c)$$

where we have introduced the parameter

$$\varrho = (1+R)\tau' + \frac{\mathcal{H}'}{\mathcal{H}} - 1. \quad (65)$$

In the tight coupling regime we use the initial conditions given in Eq. (59). We then solve the ODEs given in Eq. (58), but compute  $\Theta_1'$  and  $v_b'$  in the end by using Eq. (64). In this regime we use Eqs. Eq. (60a) and (60b) for  $\Theta_2$  and  $\Theta_\ell$ , respectively.

Next, we need to determine when the tight coupling approximation is valid. We use the same conditions as Callin, namely that the approximation holds as long as  $|\tau'| > 10$  and  $|k/\mathcal{H}\tau'| < 1/10$ , and that it should not be used after the start of recombination. For the latter condition, we choose  $x < -8.3$  as the time when recombination starts. If any of these three conditions fails, we switch to the full ODEs. We then use the final results from the tight coupling regime as initial conditions for the ODEs in Eq. (58), and integrate up to  $x = 0$ .

#### 4.2.2. Integration details (working title)

**Write about details regarding integration**

When solving the perturbation ODEs we integrate across  $x$  for each mode  $k$ , where we choose  $N_k = 100$  values of  $k \in [5 \cdot 10^{-5}, 0.3]/\text{Mpc}$  values. For the highest multipole, we choose  $\ell_{\max} = 7$ . As previously mentioned, we only use the higher multipoles to get an accurate result for  $\Theta_0 - \Theta_2$ . Higher multipoles are therefore not splined.

#### 4.2.3. Source function

For the source function, we use values of  $N_k = 100$  values of  $k$  in the same range as before, but now distributed quadratically

$$k_i = k_{\min} + (k_{\max} - k_{\min})(i/N_k)^2, \quad (66)$$

#### 4.3. Results

**I will later add lines to the plots below, showing where  $k\eta = 1$  for the different modes.**

In this section we present plots showing the evolution of some perturbation quantities. For the monopole and dipole, we express plot these in terms of  $\delta_\gamma$  and  $v_\gamma$ , respectively. For easier comparison between evolution of baryons, photons and CDM, we plot CDM and baryons together in one figure, and baryons and photons together in another figure. In both cases we include all three modes in the same figure. This prevents cluttering of the figures, and helps understand the physics behind the three constituents, as baryons interact with both CDM and photons.

In Figs. 13-17 we indicate the time of matter-radiation equality by a dotted black vertical line. Since we have set  $\mathcal{N}_{\text{eff}} = 0$ , the matter-radiation equality we consider here occurs at  $x_{\text{eq}} = -8.6577$ , as opposed to the time given in table 2.3.3. The time of decoupling and recombination is less affected, taking place

at  $x \sim -6.98$  once again. For brevity, we will from now on refer to modes with large  $k$  as *short modes* and modes with small  $k$  as *long modes*, as they are related to small and large scales, respectively.

We begin by studying the density evolutions in Sect. 4.3.1, and spend a considerable time discussing these results, with an emphasis on interpreting the physics qualitatively. With a system of many coupled ODEs, this initial discussion will provide us with a simpler way of understanding the mechanism behind the remaining perturbation quantities.

#### 4.3.1. Density perturbations

(Mention decoupling x)

We begin by plotting the absolute value of the density evolution for the matter components and photons, shown in Fig. 13, where the upper panel shows  $\delta_{\text{CDM}}$  and  $\delta_b$  and the lower panel shows  $\delta_b$  and  $\delta_\gamma$ . We see that the baryons and CDM follow each other closely during the tight coupling regime, and that the  $\delta_b$  deviates noticeably from  $\delta_{\text{CDM}}$  during recombination for the shortest mode. On small scales we will initially have overdense regions of CDM undergoing gravitational collapse. This will attract baryons which will fall into the CDM potential wells. As baryons collapse, pressure from photons will increase and push the baryons outwards again. We see a manifestation of this process in the lower panel, where  $\delta_b$  and  $\delta_\gamma$  follow each other as a single fluid before decoupling.

This process will repeat until recombination occurs, after which the photons move freely, and baryons can collapse into the gravitational wells set up by CDM. This causes  $\delta_b$  to follow  $\delta_{\text{CDM}}$  at late times. When photons decouple from matter and move freely, their temperature are no longer affected by interactions, and we get an approximately constant  $\delta_\gamma$  towards  $x = 0$ .

For the intermediate mode, oscillations starts much closer to the time of decoupling, and we therefore only see few oscillations in both panels. The large mode enters the horizon much later, with gravitational collapse taking place long after decoupling. Neglecting terms with factors of  $k$  in Eq. (58), we get  $\delta_b = \delta_{\text{CDM}}$  at all times, since they have identical initial conditions.  $\delta_\gamma$  on the other hand deviates from  $\delta_b$  some time after recombination has occurred. (Fix last sentence, explain onset of photon decoupling).

The value of  $\delta_\gamma$  after decoupling differs between the three modes, where shorter modes have a lower final value of  $\delta_\gamma$ , i.e. a lower temperature. The gravitational wells are dominated by CDM before decoupling. On small scales CDM will have more time to cluster before decoupling, and is the reason for why we have  $\delta_{\text{CDM}}$  is larger for at a given  $x$  for shorter modes. When photons decouple they are redshifted as they climb out of gravitational wells, causing a reduction in their temperature. This redshift is stronger for short modes where  $\delta_{\text{CDM}}$  is higher, and explains the different values of  $\delta_\gamma$  we see at late times for the three modes. **Make distinction between gravitational potential and overdensities!**

As we have seen, the decoupled photons are affected by how much a given mode has clustered. The total amount of clustering before decoupling is related to when decoupling happens. However, another crucial factor is how the clustering evolves for the different modes. For the shortest mode, we see that  $\delta_{\text{CDM}}$  grows differently before and after  $x_{\text{eq}}$ . This is a consequence of the expansion of the Universe slowing down the growth of structure, which we will discuss in more detail in Sect. 4.3.3. For the two shorter modes we see this effect near  $x = 0$ , as the perturbations

begins to flat out when the Universe becomes dominated by dark energy, where the expansion accelerates.

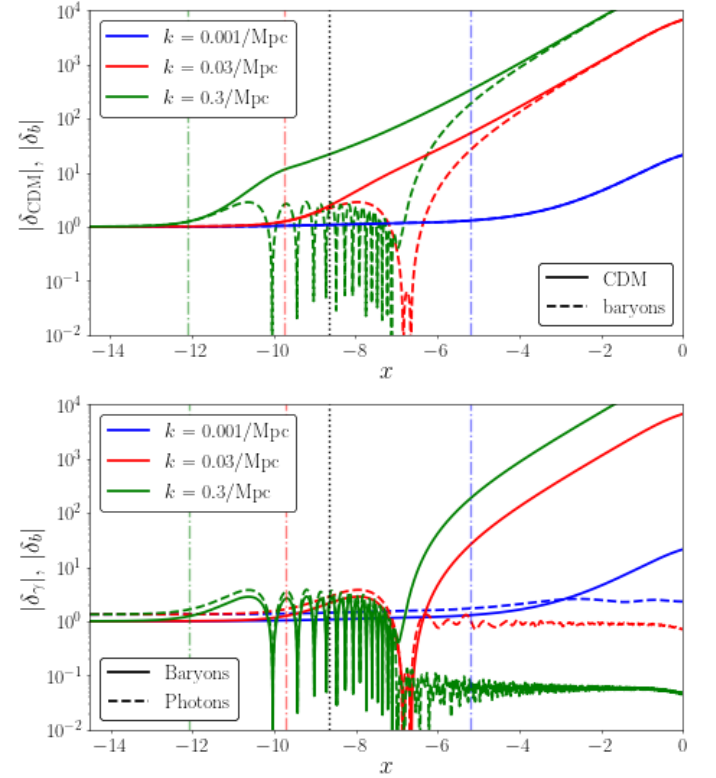


**Fig. 13.** Evolution of  $\delta$  for modes with three different wavenumbers. Upper panel: Comparing  $\delta_{\text{CDM}}$  (solid line) and  $\delta_b$  (dashed line). Lower panel: Comparing  $\delta_b$  (solid line) and  $\delta_\gamma = 4\Theta_0$  (dashed line).

#### 4.3.2. Velocity perturbations

The evolution of the velocities is shown in Fig. 14, where we compare baryons and CDM in the upper panel, and baryons and photons in the lower panel. Note that we have used a linear scale for the lower panel to reduce clutter.

The oscillating behaviour displayed by baryons for short modes in Fig. 13 is evident for the velocities, where the velocity extrema coincides with density minima, as expected. For  $v_b$  and  $v_{\text{CDM}}$  we see similar behaviour as we did for the densities, where baryons and CDM coincide towards early and late times, with decoupling effects in the middle for the two shorter modes. For the longest mode we have  $v_{\text{CDM}} = v_b$ , following the same argument as we did for their densities. One major difference, is that the acceleration of the matter components,  $v'$ , has become negative near  $x = 0$ .

For the shortest mode,  $v_{\text{CDM}}$  is no longer a strictly increasing function at early times. Around  $x = -10$ ,  $v_{\text{CDM}}$  declines and becomes smaller than the intermediate mode around  $x_{\text{eq}}$ <sup>4</sup>.

During tight coupling we have  $v_b \sim v_\gamma$ , and near decoupling, at  $x \sim -7$ , we see that the photons decouple from the plasma. After that, the photons undergo damped oscillations, with a higher frequency for shorter modes.

<sup>4</sup> I have no sensible explanation for this

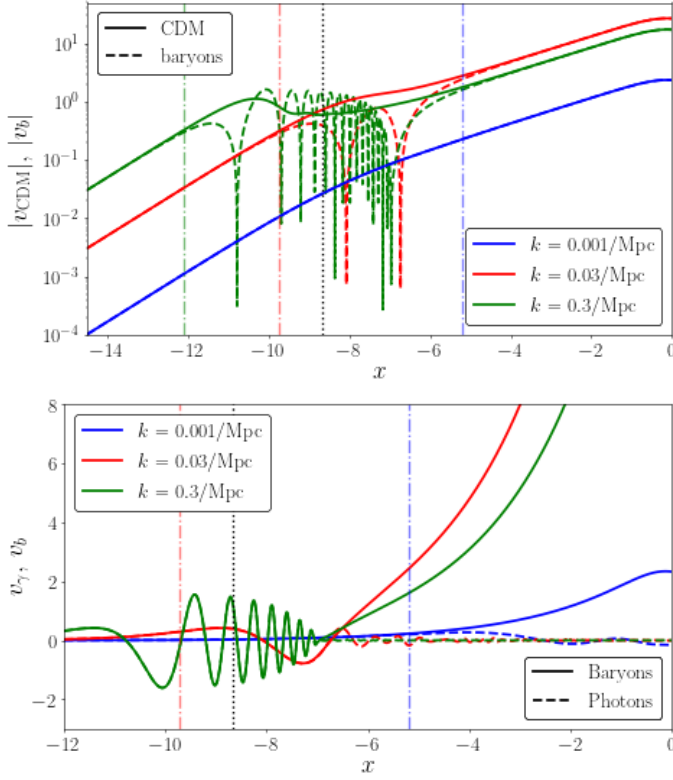


**Fig. 14.** Evolution of velocities for three different wavenumbers. Upper panel:  $v_{\text{CDM}}$  (solid line) compared to  $v_b$  (dashed line). Lower panel:  $v_b$  (solid line) compared to  $v_\gamma$  (dashed line).

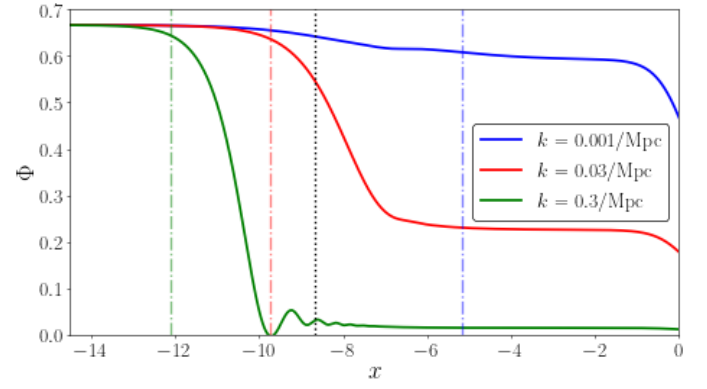


**Fig. 15.** Evolution of  $\Phi$ .

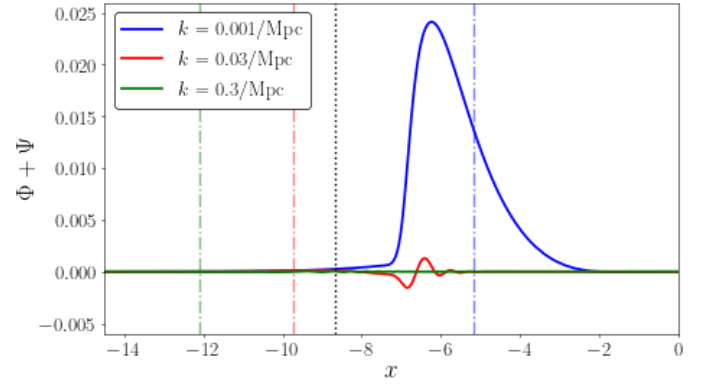


**Fig. 16.** Evolution of the combined metric perturbations,  $\Phi + \Psi$

#### 4.3.3. Potential perturbations

The evolution of  $\Phi$  is shown in Fig. 15. The following discussion is based upon the results of (Dodelson 2020, Ch. 8). During both matter domination and radiation domination,  $\Phi$  is well approximated as being constant. The shortest mode enters the horizon when  $x \ll x_{\text{eq}}$ , and once it does so, as a result the potential decays and begins to oscillate. This behaviour gives rise to the damped oscillations for photons and baryons in Fig. 13. During matter domination we get constant  $\Phi$  when a mode has entered the horizon, as matter accretion is balanced by the expansion of the Universe.  $\Phi$  is then balanced by the expansion of the Universe and the accretion of matter. The constant  $\Phi$  explains why all modes in Fig. 13 grow at the same rate at late times, long after decoupling. There is a transition period between the two constant  $\Phi$  regimes during matter and radiation domination, which coincides with times when the densities grow at different rates around  $x_{\text{eq}}$ . Towards  $x = 0$ , we get a notable decrease in  $\Phi$  for all modes, which is due to dark energy domination causing an accelerated expansion.

In Fig. 16 we plot the sum of the two metric potentials,  $\Phi + \Psi$ , which corresponds to the second term on the RHS of Eq. (58j). We therefore have  $\Phi + \Psi \propto -\Theta_2/k^2 \cdot e^{-2x}$ , and is thus proportional to the quadrupole moment,  $\Theta_2$ , which is shown in Fig. 17. Since  $\Theta_2(x \ll x_{\text{eq}}) \approx 0$ , the sum of the potentials is zero initially. The proportionality constant is very small, and so for larger  $x$ , late in the matter dominated era, there is no contribution from the potential sum. This gives only a narrow range where both  $\Theta_2$  contributes and the exponent is large enough to give a contribution. **Rewrite paragraph.**

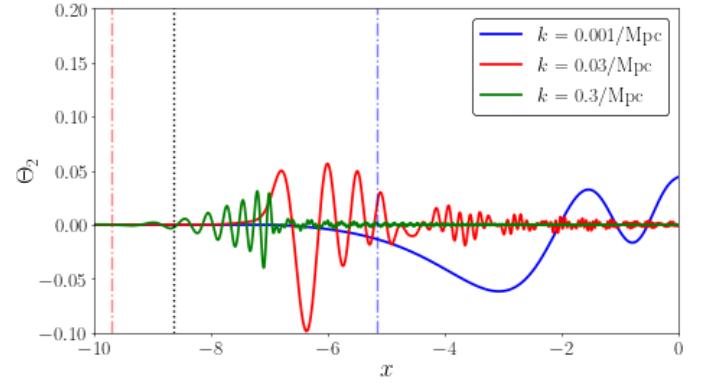


**Fig. 17.** Evolution of the quadrupole,  $\Theta_2$ . At  $x < -10$ , there is no apparent contribution of this quantity.

## 5. Milestone IV

Some introduction about what it is all about.

### 5.1. Theory

The theory behind this milestone.

### 5.2. Implementation details

Something about the numerical work.

### **5.3. Results**

Show and discuss the results.

## **6. Conclusions**

Write a short summary and conclusion in the end.

*Acknowledgements.* I thank my mom for financial support!

## References

- Betoule, M., Kessler, R., Guy, J., et al. 2014, A&A, 568, A22, doi: 10.1051/0004-6361/201423413
- Callin, P. 2006, arXiv e-prints, astro, doi: 10.48550/arXiv.astro-ph/0606683
- Dodelson, S. 2020, Modern Cosmology (Academic Press), doi: 10.1016/C2017-0-01943-2
- Galassi, M. e. a. 2009, GNU scientific library reference manual (Network Theory Ltd.)
- Planck Collaboration, Aghanim, N., Akrami, Y., et al. 2020, A&A, 641, A6, doi: 10.1051/0004-6361/201833910
- Seljak, U., & Zaldarriaga, M. 1996, ApJ, 469, 437, doi: 10.1086/177793
- Winther, H. A. 2023, Cosmology II: Initial conditions. [https://cmb.wintherscoming.no/theory\\_initial.php#init](https://cmb.wintherscoming.no/theory_initial.php#init)

## Appendix A: Fiducial parameters

The parameter values we use in this report are

$$\begin{aligned}
 h &= 0.67, \\
 T_{\text{CMB}0} &= 2.7255 \text{ K}, \\
 N_{\text{eff}} &= 3.046, \\
 \Omega_{b0} &= 0.05, \\
 \Omega_{\text{CDM}0} &= 0.267, \\
 \Omega_{k0} &= 0, \\
 \Omega_{\nu0} &= N_{\text{eff}} \cdot \frac{7}{8} \left( \frac{4}{11} \right)^{4/3} \Omega_{\gamma0}, \\
 \Omega_{\Lambda0} &= 1 - (\Omega_{k0} + \Omega_{b0} + \Omega_{\text{CDM}0} + \Omega_{\gamma0} + \Omega_{\nu0}), \\
 n_s &= 0.965, \\
 A_s &= 2.1 \cdot 10^{-9}, \\
 Y_p &= 0.245, \\
 z_{\text{reion}} &= 8, \\
 \Delta z_{\text{reion}} &= 0.5, \\
 z_{\text{Hereion}} &= 3.5, \\
 \Delta z_{\text{Hereion}} &= 0.5,
 \end{aligned} \tag{A.1}$$